



Effect of (Co and Zn) doping on structural, characterization and the heavy metal removal efficiency of CuFe_2O_4 nanoparticles

Rania Ramadan¹ · Mai M. El-Masry²

Received: 28 December 2022 / Revised: 21 June 2023 / Accepted: 23 July 2023
© The Author(s) 2023

Abstract

Nanomaterials, especially ferrites, have various applications in mechanical, electrical, and optical fields. However, their abilities in environmental applications remain unexplored. In this work, the flash auto-combustion method has been used to prepare three different compositions of CuFe_2O_4 , $\text{Zn-CuFe}_2\text{O}_4$, and $\text{Co-CuFe}_2\text{O}_4$ nanocomposite. The structure, spectroscopic, surface, and morphological properties of the prepared samples were characterized using XRD, FTIR, BET, and HRTEM, respectively. According to XRD analysis, the prepared ferrites consist of nanocrystalline particles with sizes of 24.5, 37.5, and 32.6 for CuFe_2O_4 , $\text{Zn-CuFe}_2\text{O}_4$, and $\text{Co-CuFe}_2\text{O}_4$, respectively. $\text{Zn-CuFe}_2\text{O}_4$ and $\text{Co-CuFe}_2\text{O}_4$ had a single cubic phase, while a tetragonal phase was formed in CuFe_2O_4 . The addition of cobalt and zinc to copper ferrite increased the crystallite size and the lattice parameters. The absorption band in FTIR spectra, which represents the stretching vibrations along the [MetalO] bond at the octahedral (B) position, was nearly constant (412 cm^{-1}) by the addition of Zn to CuFe_2O_4 . The surface area and quantity of gas adsorbed on the surface of $\text{Co-CuFe}_2\text{O}_4$ were the highest. The greatest force constants [$K_0 = 1.37$ & $K_T = 1.32 \cdot 10^5 \text{ dyne/cm}$] were detected in $\text{Zn-CuFe}_2\text{O}_4$. $\text{Co-CuFe}_2\text{O}_4$ exhibited the highest saturation magnetization as well as magnetocrystalline anisotropy. From FESM, the particles have a homogeneous distribution, which is confirmed by the appropriate synthesis method. The nanonanosamples had an average particle size of 79 nm, 66 nm, and 56 nm for CuFe_2O_4 , $\text{Co-CuFe}_2\text{O}_4$, and $\text{Zn-CuFe}_2\text{O}_4$, respectively. The surface area and quantity of gas adsorbed on the sample surface were increased by doping Cu ferrite with Co and Zn. All the prepared samples were tested for heavy metal (Cr^{6+}) removal from the water; they demonstrated promising results after optimizing the experimental conditions at pH 7 and contact time 50 min, and these values reached 54%, 90%, and 93% for CuFe_2O_4 , $\text{Zn-CuFe}_2\text{O}_4$, and $\text{Co-CuFe}_2\text{O}_4$ nanocomposite, respectively.

Keywords Zinc doped copper ferrite · Cobalt doped copper ferrite · XRD · HRTEM · Heavy metal removal · Kinetics and isotherm

Introduction

The current lifestyle demands the development of Earth's resources [1]. Environmental concerns began with the Industrial Revolution, with the flow of industrial wastes, either badly treated or untreated, into marine systems causing the expansion of dangerous organic and inorganic contaminants

in lakes, rivers, and coastal regions [2]. Many of these contaminants transfer to food chains owing to the non-degradation character of these materials [1–3]. The rising number of research papers published about toxicity caused by chromium ions during the last 15 years reveals efforts to explain the chromium-producing contamination. Conventional methods, such as ion exchange, chemical precipitation [4], coagulation/flocculation, electrochemical treatment, and membrane filtration succeeded in removing the trace elements [5]. These drawbacks were treated by developing new nanostructure compositions for the best possible deactivation of heavy metal removal [4–6]. Consequently, the exploration continues for structures that are more stable, that are metabolized, and that are less toxic or cleared from the body along more natural pathways [7–10]. A large selection of sorbents is presented to remove heavy metal

✉ Rania Ramadan
rramadan@cu.edu.eg

✉ Mai M. El-Masry
mai.elmasry@thebes.edu.eg

¹ Materials Science Laboratory (1), Physics Department, Faculty of Science, Cairo University, Giza, Egypt

² Basic Science Department, Higher Engineering Institute, Thebes Academy, Cairo, Egypt

elements from wastewater [11], involving nanomaterials with different types of chemical function groups and coatings [12]. Nanomaterials have unique optical, mechanical, magnetic, and chemical properties that are strongly related to size, surface, shape, and the inner structure [13]. Nanomaterials should fulfill some criteria so they can be used as adsorbents for removing the toxic elements from water [13]: sorption capacities; nontoxic; low contaminants concentration; facilitate the removal of the contaminant [14]. Until the present day, a selection of nanomaterials such as graphene, carbon nanotubes, nanometals, and polymeric sorbents met those criteria and were studied for toxic trace removal from aqueous resources [15]. One of the categories of nanomaterials strongly examined for technological applications is that of spinel ferrites, which are magnetic ceramics with the formula MFe_2O_4 , where M is a divalent cation such as Cu^{2+} , Co^{2+} , Ni^{2+} , Zn^{2+} , Mn^{2+} , or Fe^{2+} [16, 17]. The stoichiometric formula for the normal spinel is $[A][B_2]O_4$, where A is a divalent and tetrahedrally coordinated cation and B is a trivalent ion octahedrally coordinated by oxygen atoms. Spinel oxides are sometimes partially inverted, and the inversion degree is given by the parameter in $[A_1-B][AB_2]O_4$, where the squared brackets correspond to the tetrahedral and octahedral interstitial sites, respectively. Because of their structural properties, nanoferrites have been used for different technological applications, such as humidity sensors, microelectronics, solar cells, catalysis, and magnetic resonance imaging (MRI) [17–20]. In addition to being significantly less toxic than silver nanoparticles, they have been examined for purification applications [21]. Copper ferrite ($CuFe_2O_4$) as well as cobalt ferrite ($CoFe_2O_4$) are classified as magnetic materials [22]. Due to their chemical stability, great saturation magnetization, high coercivity, outstanding catalytic activity, large Faraday rotation, and Kerr effect, they are more interesting than other ferrites [23]. In these fabrics, the optical, magnetic, and structural properties are strongly affected by the cation distribution over the tetrahedral (A) and octahedral (B) interstitial positions [24]. This distribution of cations is dependent on the size, shape, microstructural parameters, grain, and porosity, which can all be monitored during the synthesis process [25]. Consequently, the physical properties of spinel ferrites can be controlled by applying a suitable preparation method and adjusted to achieve the ultimate structural properties for the required application [26]. Unlike ferromagnetic $CuFe_2O_4$ and $CoFe_2O_4$, normal $ZnFe_2O_4$ is considered antiferromagnetic and has a low magnetic moment in its normal condition. Consequentially, after calcination at 1100 °C, the magnetization of nanostructured $ZnFe_2O_4$ can be enhanced

by an order of magnitude [27]. $ZnFe_2O_4$ displays different properties based on the synthesis procedures, indicating a wide range of zinc ferrites [28]. As compared to nanoferrite samples made using other methods, flash auto-combustion is a process that shows promise for improving their physical characteristics. These nanoferrite samples are suggested for usage as functional materials in a variety of applications, including microwave devices, biomedical devices, and water purification [29–31]. However, many of these applications are in the purification and desalination fields. Considering these uncertainties, the aim of this work is to study the microstructural performance, magnetic, and optical characteristics of Cu ferrite nanoparticles and the effect of Co and Zn doped $CuFe_2O_4$ as a single-phase mixed ferrite with the formulas $(Co_{0.5}Cu_{0.5}Fe_2O_4)$ and $(Zn_{0.5}Cu_{0.5}Fe_2O_4)$ for examining their efficiency for heavy metal (Cr^{6+}) removal with respect to different experimental parameters.

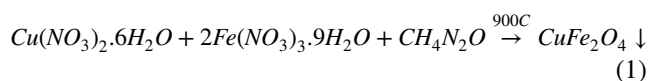
Materials and methods

Materials

Cobalt nitrate [$Co(NO_3)_2 \cdot 6H_2O$], copper nitrate [$Cu(NO_3)_2 \cdot 6H_2O$], zinc nitrate [$Zn(NO_3)_2 \cdot 6H_2O$], iron nitrate [$Fe(NO_3)_3 \cdot 9H_2O$], urea [CH_4N_2O], and ammonia solution (33%) were purchased from LOBA, India. All materials were used without further purifications.

Synthesis MFe_2O_4 ; [M = Cu, Zn-Cu, Co-Cu]

Due to the combustion method's ability to produce high-purity, homogenous, and crystalline ceramic powders, various researchers have recently employed it to synthesize Cu-ferrite, Co-ferrite, Zn-ferrite, and related ferrite systems. Nanosamples of copper, cobalt-copper, and zinc-copper ferrites were synthesized using the Flash auto-combustion procedure. The identified amounts of the raw materials, containing nitrates of cobalt (0.1 M), copper (0.1 M), zinc, and iron (0.1 M), are related to the stoichiometric ratios of the specific ferrites. These precursors, together with urea (0.7 M), were mixed up in powder form, and later a few amounts of distilled water were slowly added under strong stirring to get a dissolved mixture. Next, the temperature was raised to 250 °C until all fumes ended. This process can be expressed for $CuFe_2O_4$, Zn-Cu Fe_2O_4 , and Co-Cu Fe_2O_4 compositions using the following equations:





After that, the obtained products were calcined for 2 h at 900 °C with rate of 5 °C/min. Figure 1 illustrates the sequence of steps during the process of synthesis.

XRD measurements

The XRD study was carried out on an X-ray diffractometer (analytical-x' pertpro, Cu $k_{\alpha 1}$ radiation, $\lambda = 1.5404 \text{ \AA}$, 45 kV, 40 mA, Netherlands). The patterns were obtained within the Bragg angle (2θ) range of 4–60°. The crystallite size was computed using Scherrer's equation [29]:

$$D = \frac{k\lambda}{\beta_{\text{hkl}}\cos\theta} \quad (4)$$

where D is the crystallite size in nm, k is the shape factor (0.9), λ is the X-rays wavelength, while β_{hkl} reveals to the full width at half maximum (FWHM) in radians, and θ is the diffraction Bragg angle.

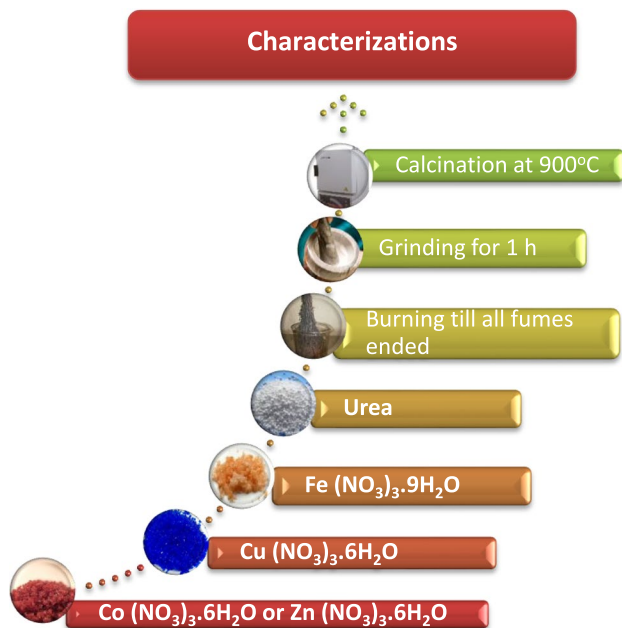


Fig. 1 Flow chart of synthesizing nano ferrites at different structure

FTIR measurements

A FT-IR spectrometer (Perkin-Elmer 2000) in the wavenumber range of 4000–400 cm^{-1} was used for measuring Fourier transformed infrared (FT-IR) spectra.

Particle morphology

High-resolution transmission electron microscopy (HRTEM, JEOL/JME 2100) was used to study the microstructure and morphology of CuFe_2O_4 , $\text{Zn-CuFe}_2\text{O}_4$, and $\text{Co-CuFe}_2\text{O}_4$ nano nanocomposite. The operating voltage was 200 kV.

Surface area analysis (BET)

The surface area and pore volume was measured by the N_2 absorption technique by using a BET Multi-point (St 2 on NOVA touch 4LX [s / n:17016062702]).

X-ray photoelectron spectroscopy (XPS)

X-ray photoelectron spectroscopy (XPS) spectra were obtained using a spectrometer (model Thermo Scientific K-Alpha) with a monochromatic X-ray source of AlK α . The measuring parameters were adjusted as 10 min, 0.100 eV, 601 and 400 lm for the acquisition time for all samples, energy step size for the analyzer mode (CAE: Pass Energy 50.0 eV), number of energy steps, and spot size, respectively, while the lens mode was standard.

Magnetic properties

The magnetic behavior of the prepared samples was examined by using a vibrating-sample magnetometer (VSM) at room temperature, and the applied magnetic field was varied up to 20 kOe.

Heavy metal removal study

To study the adsorption of Cr^{6+} onto MFe_2O_4 , [M = Cu, Zn-Cu and Co-Cu], 0.1 g of adsorbent (MFe_2O_4) was added to 100 mL of heavy metal standard solution (2 ppm) and then mixed for an hour by using the electric shaker. To investigate the effect of pH (2–10) drops of NH_4OH or HNO_3 was added to the aqueous solution. The effect of contact time was studied by adjusting pH of solution to its optimum value which obtained from part I, after each 1 h, the removal efficiency was tested till 24 h. The adsorption efficiency was determined by the following equation [30]:

$$\text{Removal(adsorption)efficiency}\% = \frac{C_0 - C_f}{C_0} \times 100\% \quad (5)$$

where:

C_0 : heavymetalsoln.atinitialconcentration(ppm)

C_f : heavymetalsoln.atfinalconcentration(ppm)

The adsorption capacity was investigated by the following equation [31]:

$$q_e = \frac{(C_0 - C_f)V}{m} \times 100\% \quad (6)$$

where:

C_0 and C_f are the initial and final concentrations of heavy metal in the solution, m is the adsorbent amount (g), V is the solution volume (L).

Adsorption isotherms

There are two isotherm models which are Langmuir and Freundlich models [32] were used for studying and calculating the adsorption parameters. Langmuir and Freundlich can be expressed by Eqs. (7) and (8) respectively.

$$\frac{C_e}{q_e} = \frac{1}{k_l q_m} + \frac{C_e}{q_m} \quad (7)$$

$$\ln q_e = \ln k_f + \frac{1}{n} \ln C_e \quad (8)$$

where:

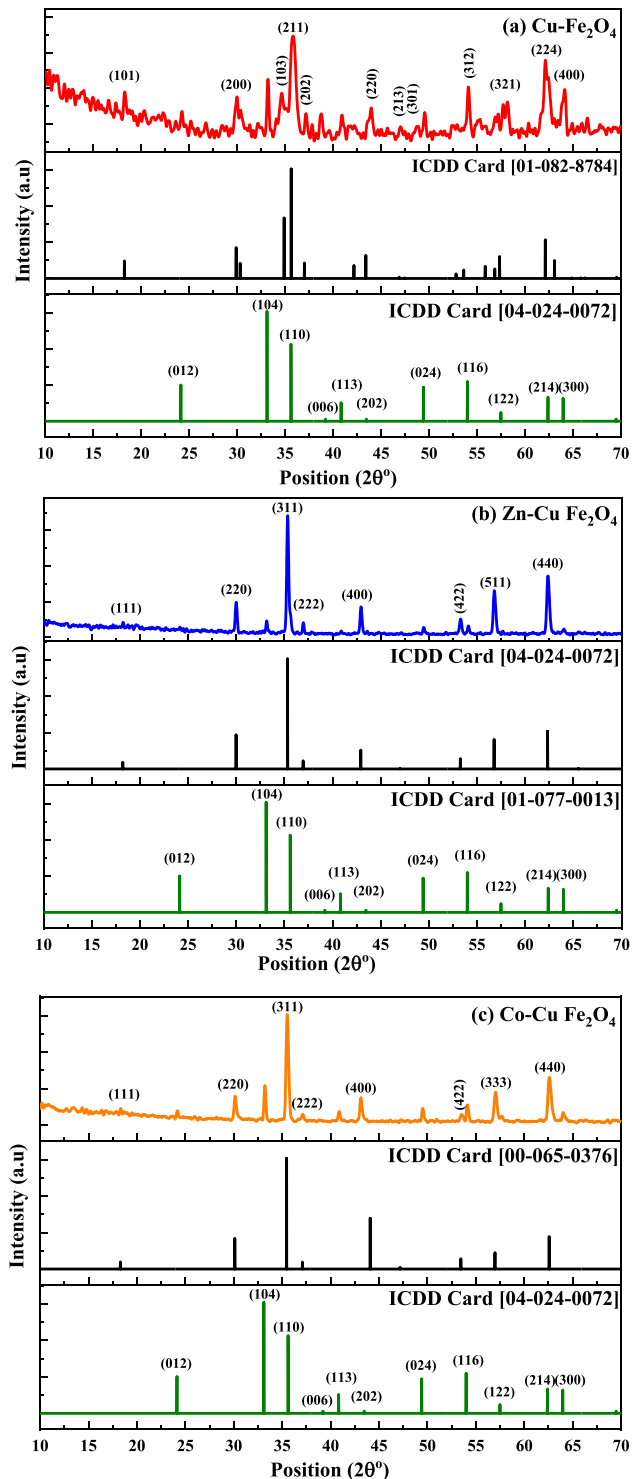


Fig. 2 XRD spectra for CuFe_2O_4 , $\text{Co-CuFe}_2\text{O}_4$ and $\text{Zn-CuFe}_2\text{O}_4$

Table 1 The average crystallite sizes, and lattice parameters of CuFe₂O₄, Co-CuFe₂O₄, Zn-CuFe₂O₄

Composition	Crystallite size (nm)	Lattice parameter (Å°)
CuFe ₂ O ₄	25	$a = b = 5.89$ and $c = 8.56$
Zn-CuFe ₂ O ₄	38	8.41
Co-CuFe ₂ O ₄	33	8.39

Where q_e and q_m (mg g⁻¹) are the adsorption capacity at equilibrium and maximum adsorption respectively, and K_f (L mg⁻¹) is the affinity binding constant. while K_j and n are physical constants signifying the adsorption capacity and intensity of adsorption, respectively.

Adsorption kinetics

To examine the adsorption kinetics mechanism, three models could be applied [31, 32]:

$$\text{Pseudofirst - order model : } \ln(q_e - q_t) = \ln q_e - \frac{k_1}{2.303} t \quad (9)$$

$$\text{Pseudosecond - order model : } \frac{t}{q_t} = \frac{1}{k_2 q_e^2} + \frac{t}{q_e} \quad (10)$$

$$\text{Interparticlediffusionmodel } q_t = k_3 t^{1/2} + C \quad (11)$$

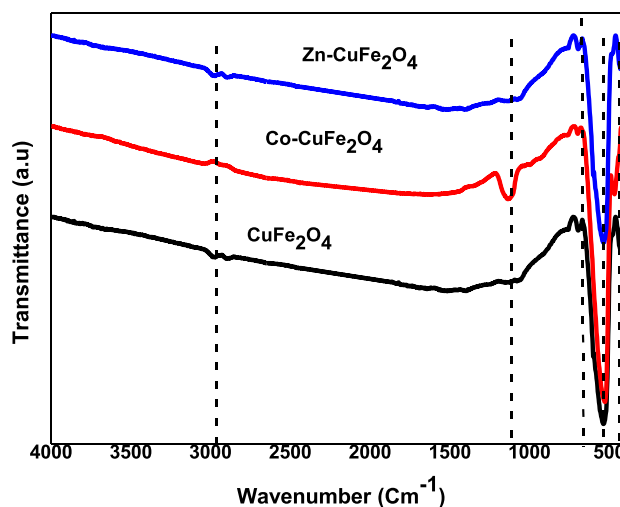
where k_1 , k_2 and k_3 are the pseudo first, second order and inter particle diffusion rate constants in (min⁻¹) and (g mg⁻¹ min⁻¹), respectively.

To ascertain the model that presented a better fit of the experimental data, each model was estimated in terms of the difference between the experimental and calculated adsorption capacity values and the correlation coefficient (R²) obtained.

Results and discussion

Crystal structure

Figure 2 shows X-ray diffraction patterns of samples of CuFe₂O₄, Zn-CuFe₂O₄, and Co-CuFe₂O₄ nanopowder. All samples showed single phases according to the ICDD cards [01-08208784], [01-077-0013], and [00-065-0376] of CuFe₂O₄, Zn-CuFe₂O₄, and Co-CuFe₂O₄, respectively. Zn-CuFe₂O₄ and Co-CuFe₂O₄ had a single cubic phase, while a tetragonal phase was formed in CuFe₂O₄. The average crystallite sizes and lattice parameters of prepared powders were estimated and listed in Table 1. It is seen that the prepared ferrites consist of nanocrystalline particles with sizes of 24.5, 37.5, and 32.6 nm for CuFe₂O₄, Zn-CuFe₂O₄, and Co-CuFe₂O₄, respectively. The results reveal that the

**Fig. 3** FTIR spectra for CuFe₂O₄, Co-CuFe₂O₄ and Zn-CuFe₂O₄

addition of cobalt and zinc to copper ferrite increased the crystallite size and the lattice parameters. The largest values were obtained for Zn-CuFe₂O₄. ICDD Card [04-024-0072] belongs to hematite, which appeared in the investigated samples in two different peaks.

FTIR spectra

For ferrites, there are primarily two types of absorption bands. The first group, which is associated with the octahedral site (u1), has an absorption range of 400 to 460 cm⁻¹, whereas the second group is linked to the tetrahedral site (u2) and has a range of 480 to 600 cm⁻¹ [33].

Figure 3 displays the FTIR ranges for Co-Cu ferrite and Zn-ferrites, and while the position of the most major spectral lines was listed below in Table 2, the wavenumbers of 534.97, 598 and 934 cm⁻¹ could be attributed to the stretching vibrations at the octahedral site along the [MetalO] bond [34]. While the wavenumbers of 412.65 and 430.20 cm⁻¹ represent the stretching vibrations along the [MetalO] bond at the octahedral (B) position [34]. The u₁ band of CuFe₂O₄ is shifted to a higher wavenumber with the doping of Co, while no shift was observed in the case of Zn doping. The increase of the absorption frequencies with the substitution of lighter Co ions (Mw = 58.93 g/mol) with heavier Cu ions (Mw = 63.546 g/mol) (Table 2) led to an increase in the average mass of the metallic ions involved in the stretch. The absorption band, which represents the stretching vibrations along the [MetalO] bond at the octahedral (B) position, was nearly constant (412 Cm⁻¹) by the addition of Zn to CuFe₂O₄. This behavior can be explained by the Zn atom, which occupies the tetrahedral position; consequently, the [Metal-O] stretching vibration at the octahedral site is not affected.

Table 2 The characteristic absorption bands of FTIR spectra CuFe₂O₄, Co-CuFe₂O₄, Zn-CuFe₂O₄. All values represent wavenumbers [cm⁻¹]

	CuFe ₂ O ₄	Co-CuFe ₂ O ₄	Zn-CuFe ₂ O ₄	Assignment	Ref
	412.65	466.73	412.88	Stretching mode (ν ₁) of [M–O] bond	[33]
	534.97	526.48	533.06	Stretching mode (ν ₂) of [M–O]	[34]
	1600	1645	1650	Bending of water molecule	[35]
	2972.33	2900	2900	Vibrational mode of O–H	[36]

Table 3 The calculating force constant K_O and K_T by using ν₁ and ν₂ vibration modes

Composition	ν ₁ (cm ⁻¹)	ν ₂ (cm ⁻¹)	K _O × 10 ⁵ (dyne/cm)	K _T × 10 ⁵ (dyne/cm)
CuFe ₂ O ₄	412.65	534.97	1.031	1.217
Co-CuFe ₂ O ₄	466.73	526.48	0.827	1.179
Zn-CuFe ₂ O ₄	412.88	533.06	1.371	1.312

By knowing the values of absorption bands ν₁ and ν₂ at the octahedral (B) and tetrahedral (A) positions respectively, the force constant could be determined by using the following equations [37]:

$$K_O = 10.62 \times \left(\frac{M_{w1}}{2}\right) \times \nu_1^2 \times 10^{-3} \left(\frac{\text{dyne}}{\text{cm}}\right) \quad (12)$$

$$K_T = 7.62 \times M_{w2} \times \nu_2^2 \times 10^{-3} \left(\frac{\text{dyne}}{\text{cm}}\right) \quad (13)$$

where K_O and K_T are the force constants for the octahedral (B) and tetrahedral (A) sites, respectively, M_{w1} and M_{w2} are the molecular weights at B and A sites, respectively, while ν₁ and ν₂ represent the absorption bands corresponding to octahedral and tetrahedral sites, respectively. The calculated force constants are stated in Table 3.

It is obvious that the lowest values of K_T and K_O are significantly related to Co-CuFe₂O₄, which agrees with the molecular weight. Simultaneously, the force constant is contrary to the bond length [37]. Here, there is a particularly large increase in K_O from 1.031 × 10⁵ dyne/cm in CuFe₂O₄ to 1.371 × 10⁵ dyne/cm in Zn-CuFe₂O₄, along with an increase in K_T from 1.217 × 10⁵ dyne/cm in CuFe₂O₄ to 1.312 × 10⁵ dyne/cm in Zn-CuFe₂O₄. On the other hand, the opposite trend is observed in Co-CuFe₂O₄. Consequently, the changes to the vibration modes attributed to the transition from pure Cu ferrite to Co and Zn-doped Cu ferrite can be explained based on the crystal field, which is affected by the bond length and the cation mass. The obtained elastic parameters corresponding to the investigated samples are consistent with many reported data [38–40].

Microstructural investigation

The prepared ferrites' microstructural properties are shown in Fig. 4(a–c). Cubic nanoparticles are present in Cu-ferrite in a single phase. The suitable synthesis procedure attests to the homogenous distribution of the particles. CuFe₂O₄, Co-CuFe₂O₄, and Zn-CuFe₂O₄ had generated samples with average particle sizes of 79 nm, 66 nm, and 56 nm, respectively. These values exceeded those seen in the XRD results. Due to the prepared samples' strong magnetic characteristics, the particles clumped together to form clusters.

Surface area analysis (BET)

Referring to the data in Fig. 5a–c, it is observed that all the samples follow the type IV isotherm, which is related to the mesoporous structures [38]. The quantity of the monolayer adsorbed gas v_m on the surface of prepared samples and the BET constant were calculated and listed in Table 4 using values of slope (A) and intercept (I) obtained from the BET plot using the following equations [39]:

$$v_m = \frac{1}{A + I} \quad (14)$$

$$C = 1 + \frac{A}{I} \quad (15)$$

where: A and I are the slope and intercept of BET plot.

The observed data in Table 1 show that doping Cu ferrite with Co and Zn enhanced the surface area and amount of gas adsorbed on the sample surface. These doped samples are therefore thought to be potential materials for catalytic and adsorption applications.

Magnetic properties

Figure 6 displays the magnetic properties of CuFe₂O₄, Co-CuFe₂O₄, and Zn-CuFe₂O₄ nanoferrites. The magnetic properties of ferrites overall depend greatly on the crystal structure, cation distribution, porosity, chemical composition, grain size and grain boundary structure. The magnetic parameters obtained from the hysteresis loops (M–H) were

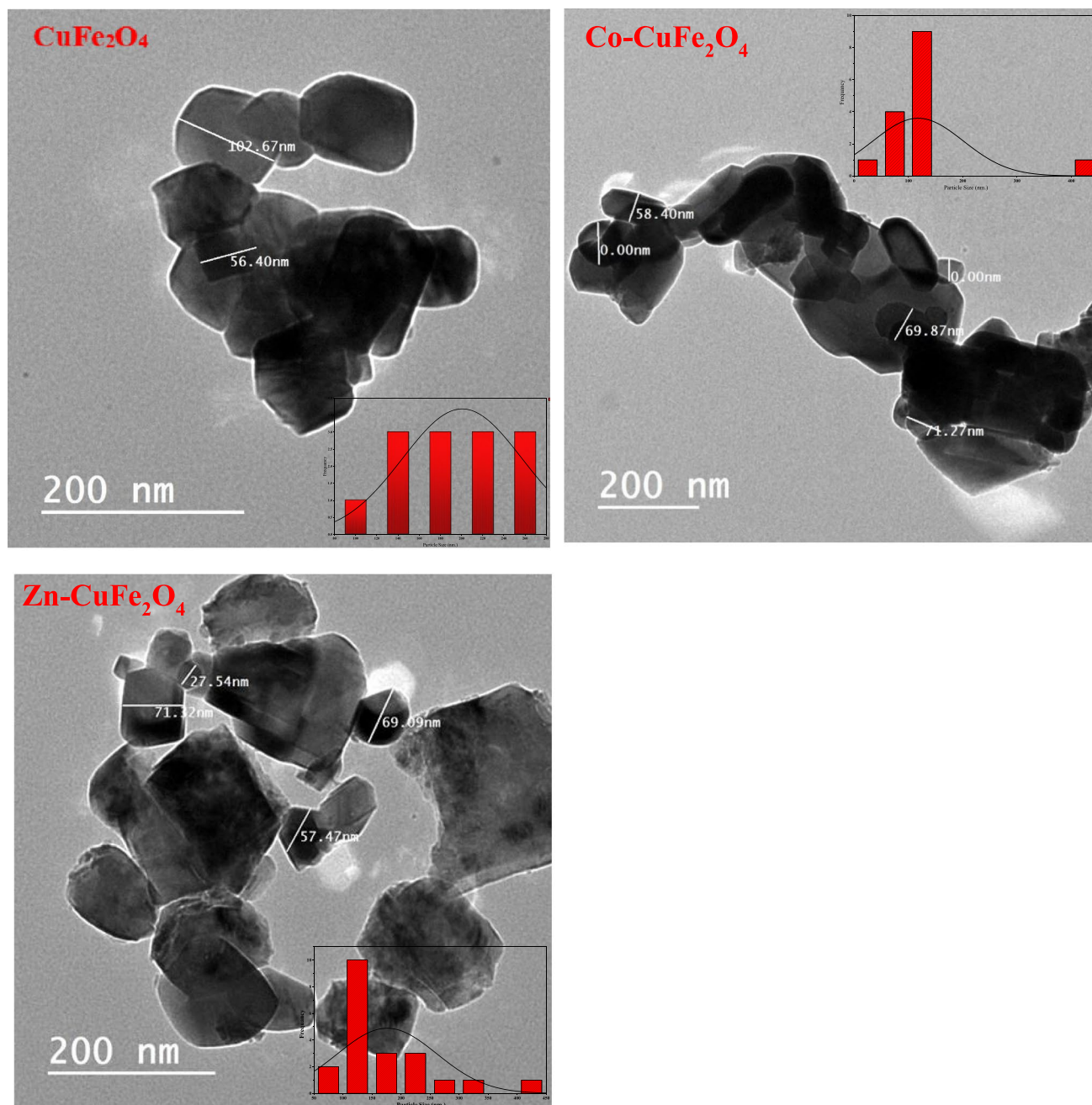
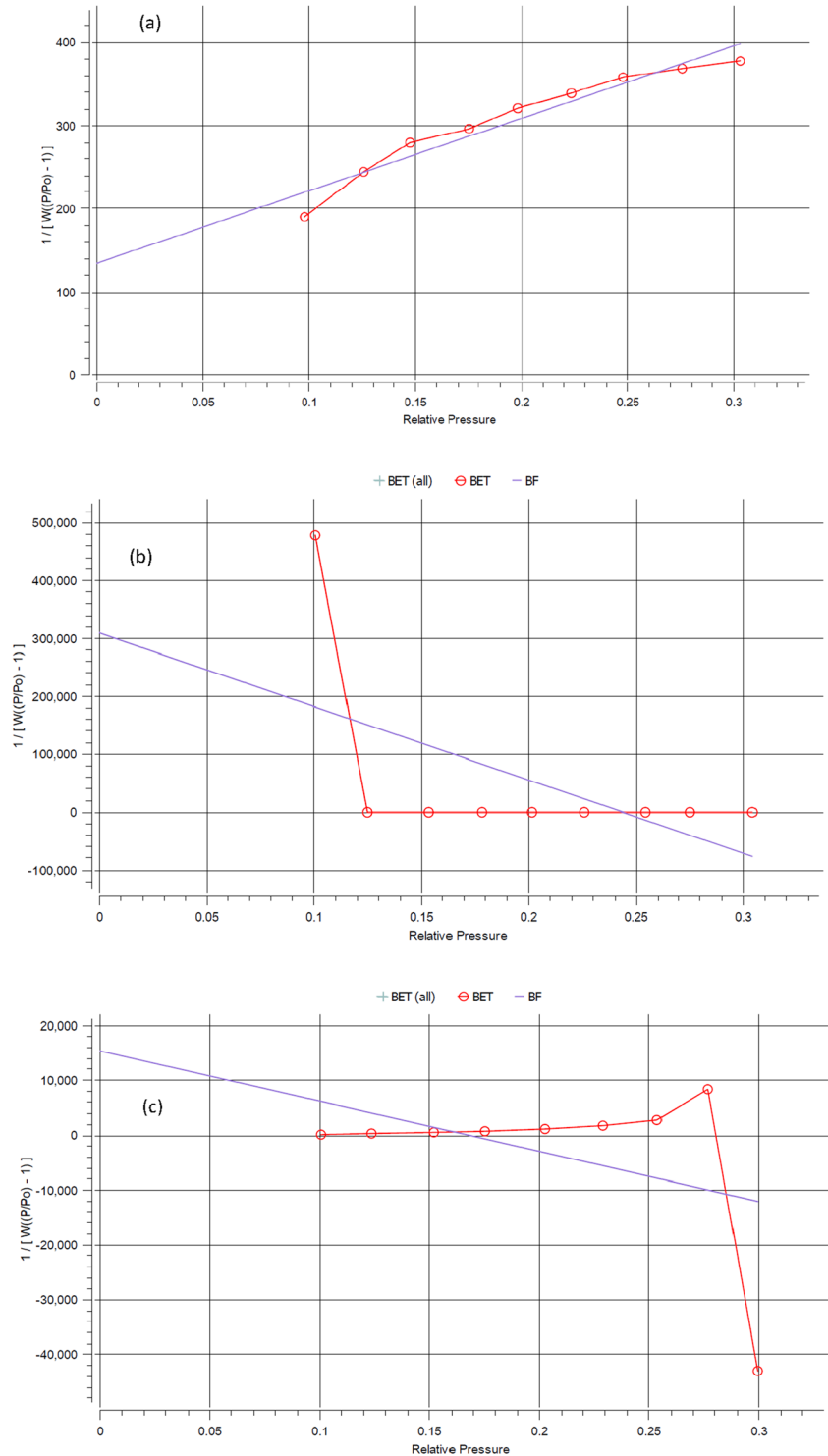


Fig. 4 (a-c) TEM micrographs of (a) CuFe_2O_4 , (b) $\text{Co-CuFe}_2\text{O}_4$ and (c) $\text{Zn-CuFe}_2\text{O}_4$

listed in Table 5. All the prepared samples follow a ferromagnetic behavior [40]. The saturation magnetization of $\text{Co-CuFe}_2\text{O}_4$ and $\text{Zn-CuFe}_2\text{O}_4$ were nearly equal to the double value of the saturation magnetization of pure Cu -ferrite. According to conventional wisdom, metallic ions interact magnetically in three different ways through direct exchange mechanisms and an indirect superexchange mechanism using intermediary oxygen ions (O^{2-}). These interactions include the A-A and B-B intra-sublattice exchange contacts

as well as the A-B superexchange interaction, where O^{2-} ions mediate the interaction because of the great separation of the metallic ions. A-B superexchange is by far the most common type of magnetic interaction among these sources of ferrimagnetism. The unpaired electron spins in these ions exhibit an antiparallel orientation due to the interaction's negative energy, and the magnetic moment that results from this can be represented by a difference between their respective magnetic moments. For $\text{Co-CuFe}_2\text{O}_4$, the higher

Fig. 5 (a-c): Brunauer–Emmett–Teller plot of (a) CuFe_2O_4 , (b) $\text{Co-Cu Fe}_2\text{O}_4$ and (c) $\text{Zn-Cu Fe}_2\text{O}_4$



value of M_s than that for pure Cu ferrite is related to the magnetic moment value. The enhancement of saturation magnetization of Zn-Cu ferrite could be explained by the inverse and normal spinel structure. From another point of view, the magnetic properties are strongly dependent on the interaction between ions in the tetrahedral (A) site and octahedral (B) site involving intermediate oxygen ions. The most

dominant type of these interactions is A-B superexchange interaction [41]. Hence, the magnetization is expressed as (Fig. 7):

$$M = |M_B - M_A| \quad (16)$$

Table 4 Quantity of monolayer adsorbed gas v_m , BET const and the surface area

Sample	V_m (Cm ³)	BET constant	surface area (Cm ² /g)
CuFe ₂ O ₄	933.521	5.099	3.46399
Co-CuFe ₂ O ₄	998.235	5.950	3.9514
Zn-CuFe ₂ O ₄	994.6795	7.447692	3.9825

where M_A and M_B represent the magnetic moment of A and B sites, usually, M_B has higher value than M_A owing to the high density of octahedral (B). In this, Zn-CuFe₂O₄, when the diamagnetic Zn²⁺ substituted Cu²⁺, it occupies the A sites, consequently, the number of Fe³⁺ ions which occupies B sites is increased leading to the net magnetization increased as well. In contrast, Co²⁺ prefers occupying B sites as Co-ferrite has inverse spinel structure, because of higher value of magnetic moment for Co²⁺ than that of Cu²⁺, the A-B super exchange interaction becomes stronger result in the net magnetization to be increased.

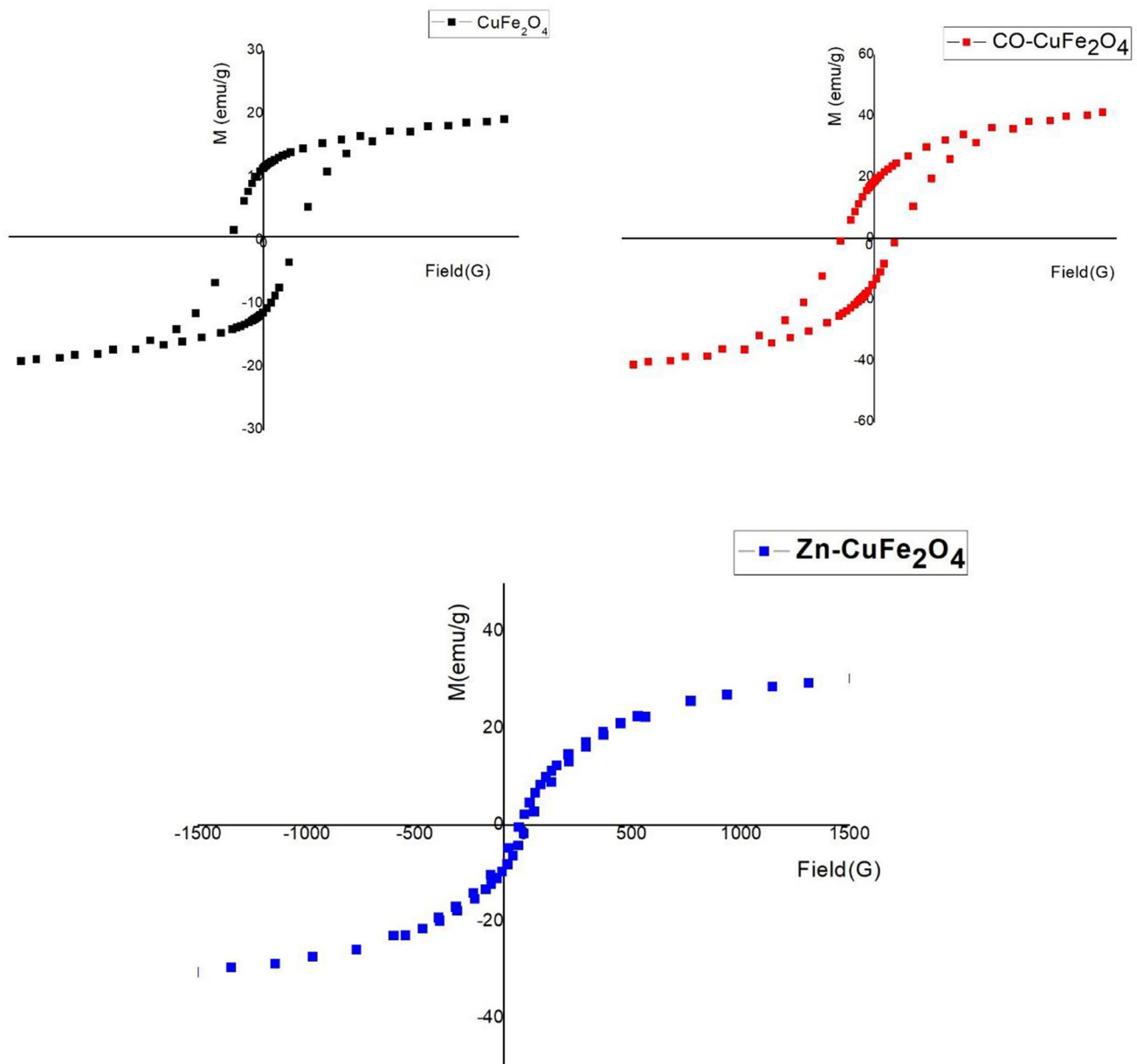
**Fig. 6** hysteresis loops of CuFe₂O₄, Zn-CuFe₂O₄ and Co-CuFe₂O₄

Table 5 Magnetic parameters, involving positive and negative saturation magnetization (M_s), coercivity (H_c), a ratio of the remnant magnetization to saturation magnetization (M_r/M_s), the exchange bias field (H_{EB}), the area of hysteresis loop for CuFe_2O_4 , $\text{Co-CuFe}_2\text{O}_4$, and $\text{Zn-CuFe}_2\text{O}_4$

Sample	M_s (+) emu/g	M_s (-) emu/g	M_s emu/g	M_r (+) emu/g	M_r (-) emu/g	M_r emu/g	M_r/M_s	H_c (+) (Oe)	H_c (-) (Oe)	H_c (Oe)	H_{EB} (Oe)	Area erg/g $\times 10^3$	Squareness
CuFe_2O_4	21.70	-21.68	21.69	11.38	-11.4	11.41	0.53	651	-648	650	0.92	45.7	0.53
$\text{Co-CuFe}_2\text{O}_4$	46.92	-46.89	46.91	16.58	-16.7	16.68	0.36	560	-550	555	4.75	80.5	0.36
$\text{Zn-CuFe}_2\text{O}_4$	38.894	-38.81	38.85	1.664	-1.92	1.793	46.2	20	-16	18	2.03	2.9	46.2×10^{-3}

More, the exchange bias (H_{EB}) of the applied field can be given by [42]:

$$H_{EB} = \frac{-[H(-) + H(+)]}{2} \quad (17)$$

where $H(-)$ and $H(+)$ are the intercepts of magnetization with the -ve and +ve on the field axis. H_{EB} has its maximum value of 4.75 Oe for $\text{Co-CuFe}_2\text{O}_4$, while its lowest value of 0.92 Oe related to pure Cu-ferrite. This behavior matches with the core@shell model for the grain structure [43]. The anisotropy constant, K (erg/g), can be expressed by [44]:

$$K = \frac{[H_c \times M_s]}{0.96} \quad (18)$$

The magnetic anisotropy is strongly affected by the coercivity; in other words, the greater the anisotropy, the higher the resistance of the dipoles to go through the annihilation under the reverse external field. From the results obtained in Table 6, it could be observed that the highest K value was calculated for Co-Cu ferrite and the lowest one was measured for Zn-Cu ferrite.

The switching field distribution (SFD), which represents the rectangularity of the M-H hysteresis loop, can be calculated by the following equation [44]. The SFD width is deeply correlated with the power of the interparticle interactions as calculated from the Delta M(H) draw.

$$\text{SFD} = \frac{\Delta H}{H_c} \quad (19)$$

where, ΔH could be calculated from the halfwidth of the dM/dH curve peak, in which sense anisotropy field (H_a) could be expected using the following equation:

$$H_a = \frac{2K}{M_s} \quad (20)$$

The coercivity and squareness of CuFe_2O_4 decreased after doping with cobalt and Zinc at room temperature to be extremely small for Zn- CuFe_2O_4 sample, these small values are characteristics of superparamagnetic nature [39, 40].

Heavy metal removal study using nano ferrites of MFe_2O_4 ; ($M = \text{Cu, Zn-Cu and Co-Cu}$)

Heavy metal ions in aqueous solutions rapidly diffuse onto the surface of the nanoferrites through the active sites. In this study, the prepared samples were used for the investigation of the removal of Cr^{6+} .

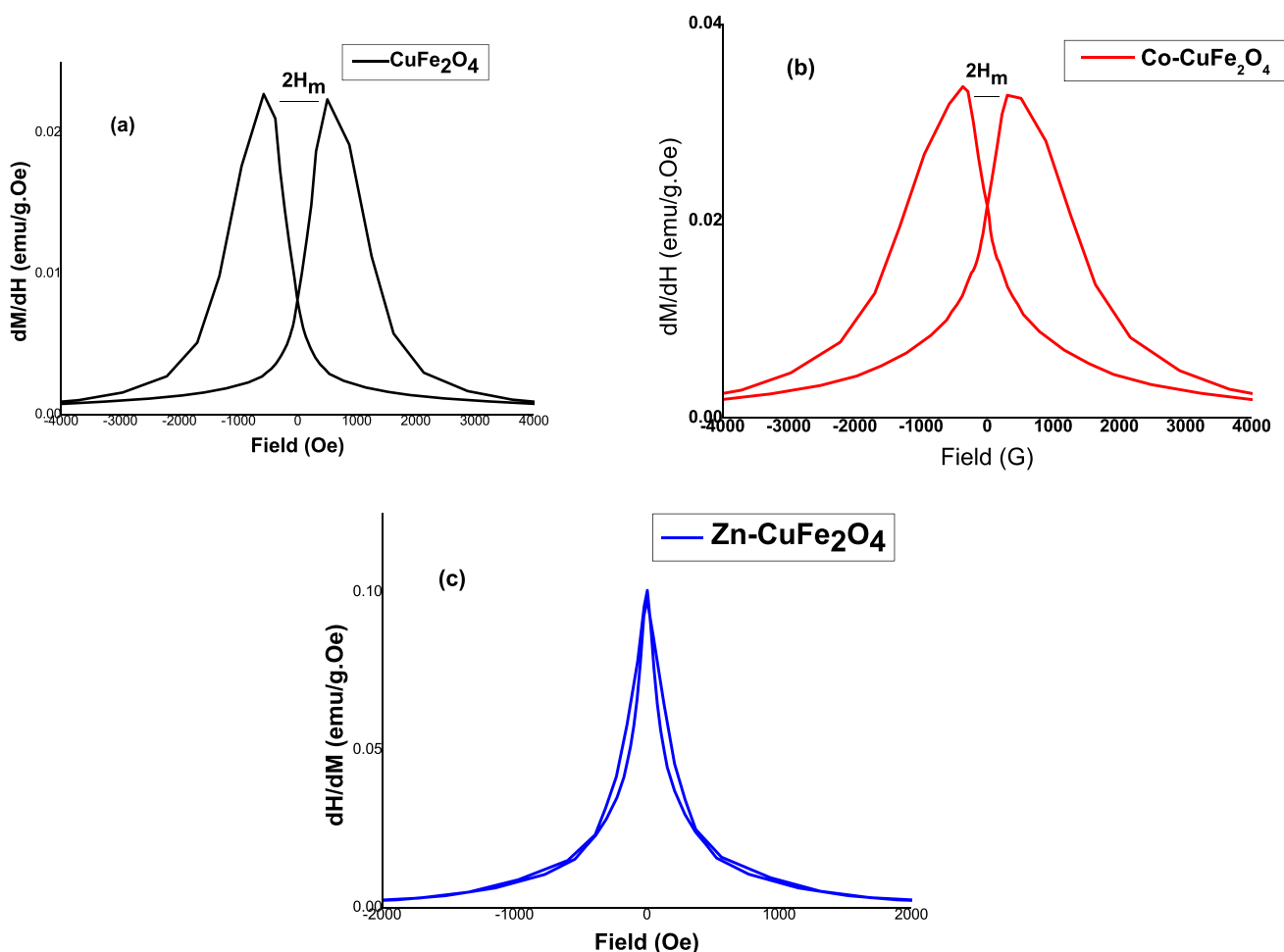


Fig. 7 Magnetic field dependence of dM/dH of (a) CuFe_2O_4 , (b) $\text{Zn-CuFe}_2\text{O}_4$ and (c) $\text{Co-CuFe}_2\text{O}_4$ and $2H_m$ measures the separation of peaks for magnetic field

Factors affecting on adsorption process

The heavy metal removal from contaminated water over various surfaces could be controlled by many factors, such as the adsorbent dosage, temperature, heavy metal ion concentration, contact time, and pH values. Hence, in this section, the effects of PH of solution and contact time were discussed, while the rest of the factors will be discussed in future work.

Table 6 The values of the magnetic anisotropy constant and anisotropy field for CuFe_2O_4 , $\text{Co-CuFe}_2\text{O}_4$ and $\text{Zn-CuFe}_2\text{O}_4$

Composition	$K \times 10^3$ (erg/g)	H_a (Oe)	SFD (Oe)
CuFe_2O_4	14.67	1.35	0.11
$\text{Co-CuFe}_2\text{O}_4$	27.12	1.15	0.26
$\text{Zn-CuFe}_2\text{O}_4$	0.732	0.037	0.16

pH effect The pH level of the aqueous medium had a significant impact on both the removal of Cr^{6+} and the adsorption capacity of the produced samples [45]. Figure 8 allows us to study how pH values affect the effectiveness of removing Cr^{6+} . Increasing the pH from 2 to 8 improved the removal efficiency for all the produced samples. This can be explained by the fact that at low pH levels, protonated function groups are present on the surfaces of the nanosamples, and that the presence of H_3O^{3+} in the medium causes competition between Cr^{6+} and H_3O^{3+} for the active sites. Furthermore, the electrostatic repulsion between the protonated function group on the sample surface and Cr^{6+} leads to difficulty in reaching the targeted heavy metal to the active sites [46]. In the case of basic medium (pH 8), at high pH values, the metal ions and OH group connected to each other, forming several complex species that blocked the active sites on the adsorbent surface. Therefore, the preferred pH for heavy metal adsorption is a moderate pH, owing to the deprotonation of the function groups at the sample's surface, which reduces the forces of

Fig. 8 Removal efficiency % as a function of pH values for MFe_2O_4 ; (M = Cu, Zn-Cu and Co-Cu)

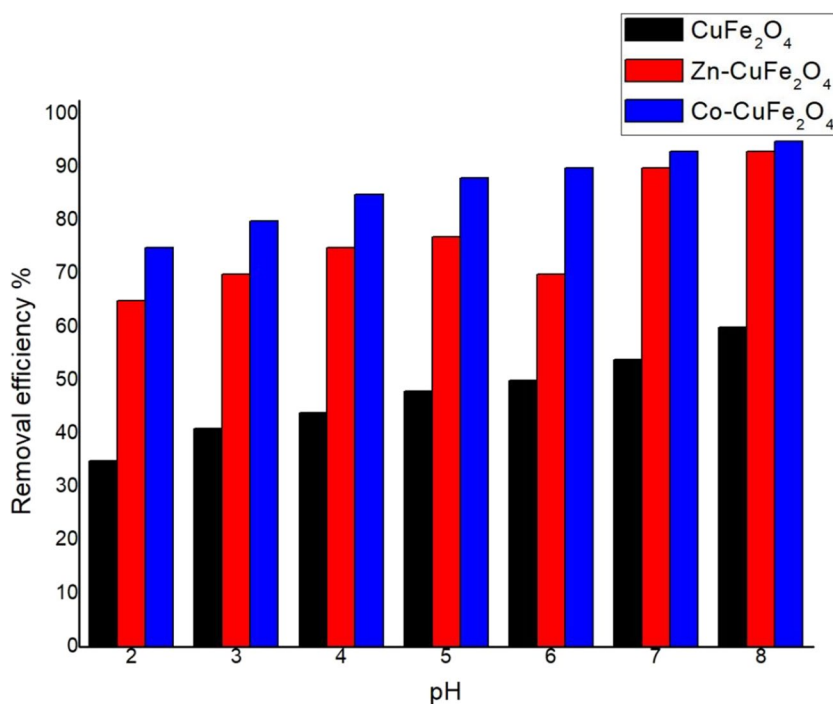
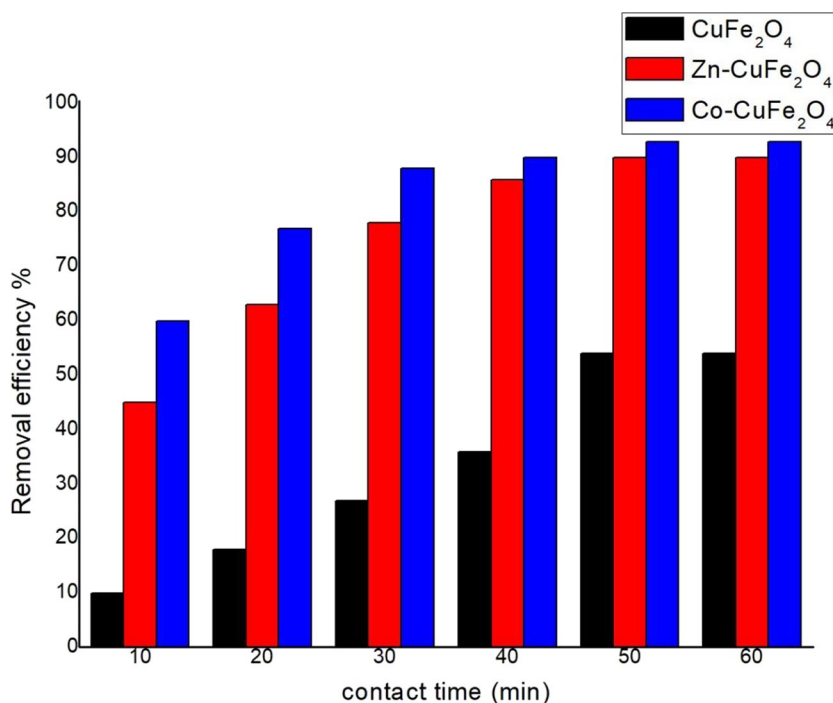


Fig. 9 Removal efficiency % as a function of contact time for MFe_2O_4 ; (M = Cu, Zn-Cu and Co-Cu)



repulsion and consequently increases the attraction of metal ions and active sites [47]. Based on the previous interpretation and the data obtained from Fig. 8, the optimum value for adsorption of Cr^{6+} was observed at pH 7, as the values of the removal efficiency were 54%, 90%, and 93% for $CuFe_2O_4$, $Zn-CuFe_2O_4$, and $Co-CuFe_2O_4$, respectively.

Contact time effect The amount of time that the adsorbent and adsorbate are in touch with one another affects how well harmful metal ions may be removed from wastewater. Due to the longer interaction time between the heavy metal ions and the active sites of the adsorbate, increasing the contact time would increase the removal effectiveness [48]. Figure 9 demonstrates

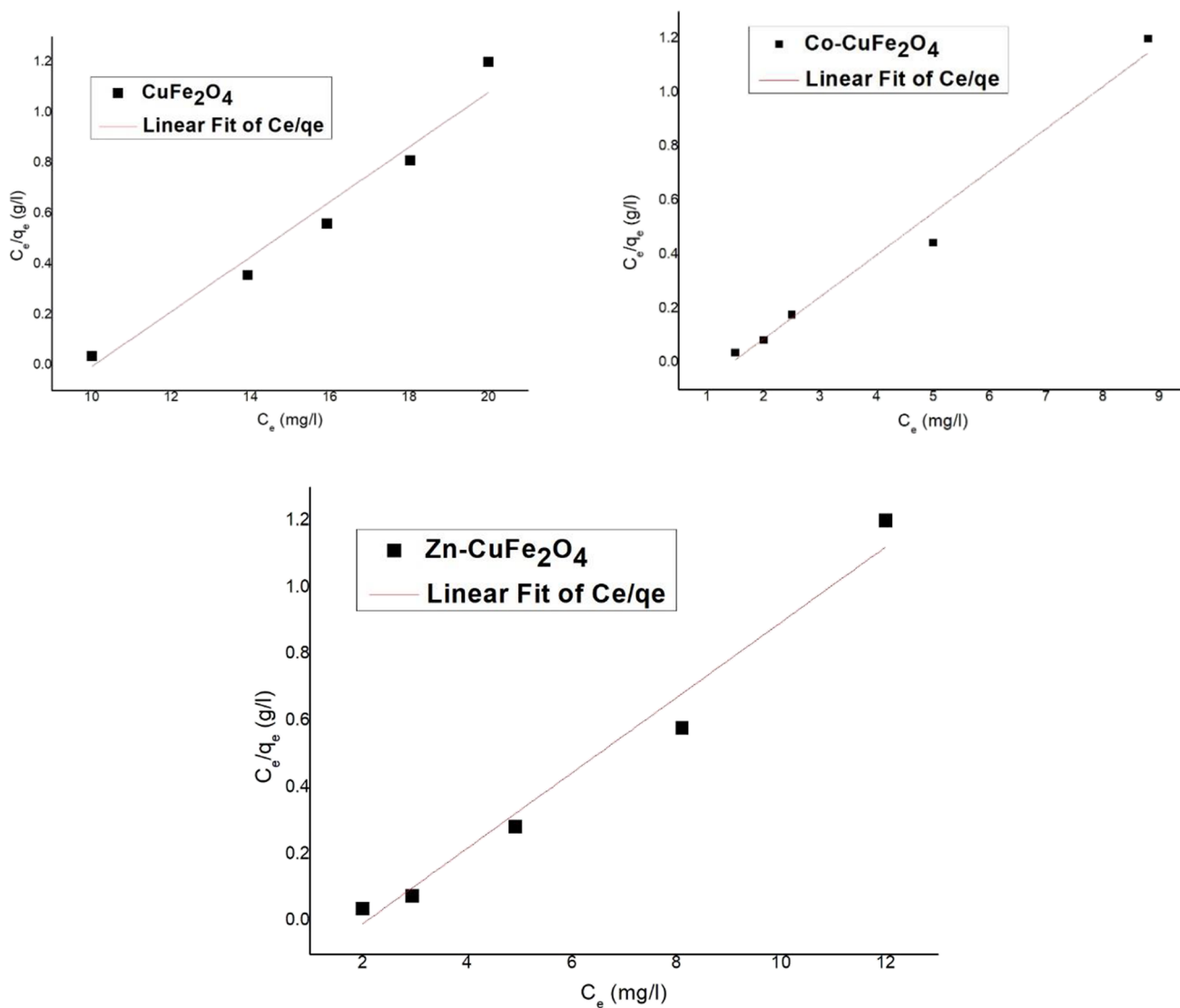


Fig. 10 Langmuir isotherm for MFe_2O_4 ; (M=Cu, Zn-Cu and Co-Cu)

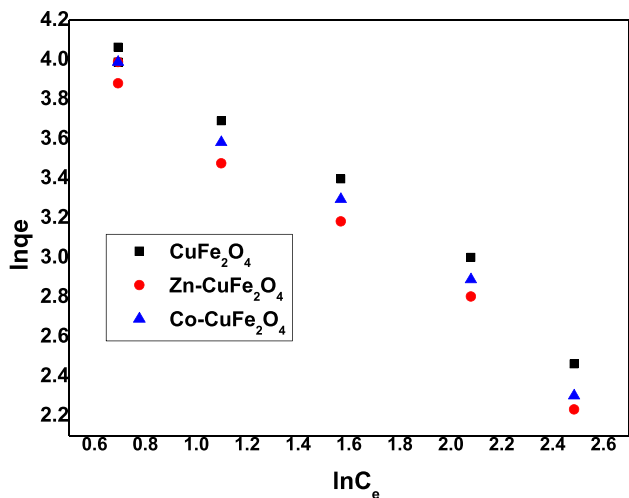


Fig. 11 Freundlich isotherm for MFe_2O_4 ; (M=Cu, Zn-Cu and Co-Cu)

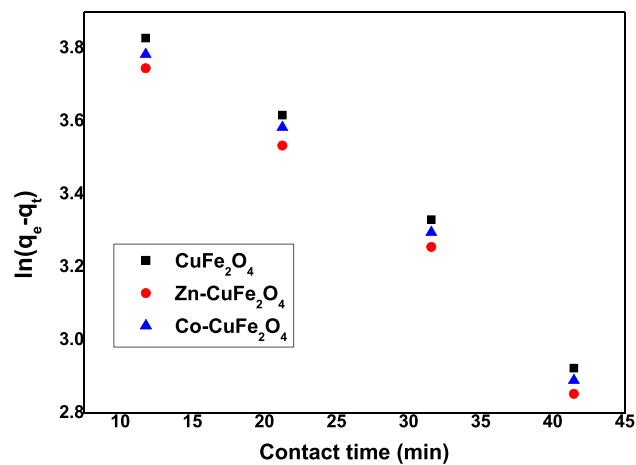


Fig. 12 Pseudo-first order model for MFe_2O_4 ; (M=Cu, Zn-Cu and Co-Cu)

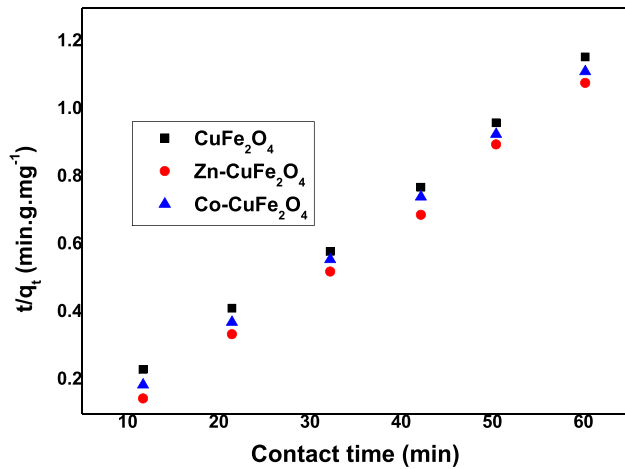


Fig. 13 Pseudo-second order model for MFe_2O_4 ; ($M = Cu, Zn-Cu$ and $Co-Cu$)

that for $CuFe_2O_4$, $Zn-CuFe_2O_4$, and $Co-CuFe_2O_4$, respectively, the removal efficiency improved quickly from 10%, 45%, and 60% at a contact time of 10 min to 13%, 63%, and 77% at a contact time of 20 min. The removal efficiency then gradually rose during the next 30 min, reaching a maximum of 54%, 90%, and 93% for $CuFe_2O_4$, $Zn-CuFe_2O_4$, and $Co-CuFe_2O_4$, respectively. At 50 min after that, there was no further increase in the removal of Cr^{6+} . This can be explained by the availability of the active sites at the beginning of the adsorption process, which are gradually occupied by the heavy metal ions with time. At the end, we conclude that the maximum adsorption of Cr^{6+} occurred by using $Co-CuFe_2O_4$ as an adsorbent at pH 7 and after a contact time of 50 min. Based on the previous results, it was expected that $Co-CuFe_2O_4$ would have the highest removal efficiency due to its high surface area and saturation magnetization.

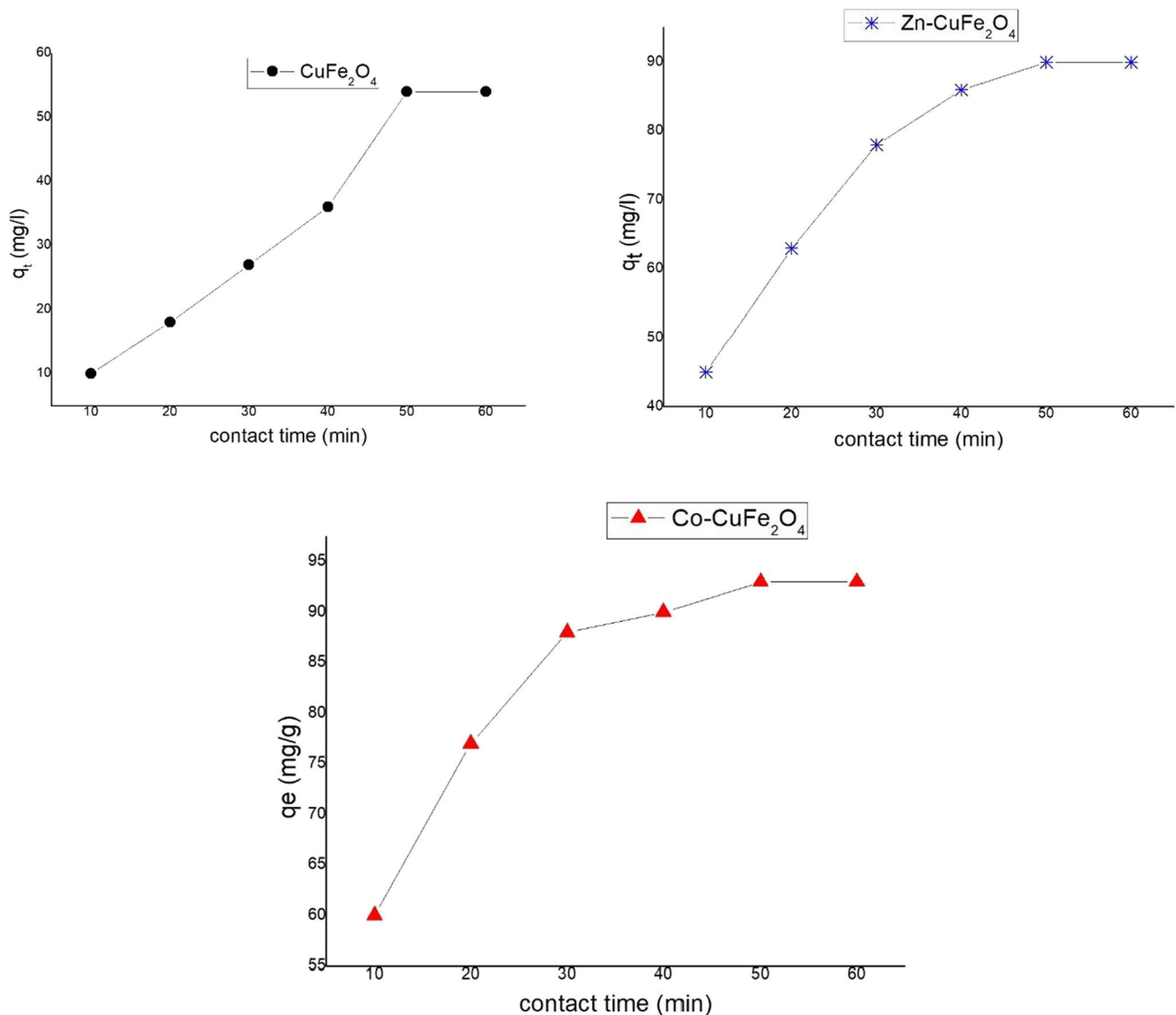


Fig. 14 Intra-particle diffusion model for MFe_2O_4 ; ($M = Cu, Zn-Cu$ and $Co-Cu$)

The adsorption isotherm The Langmuir and Freundlich isotherms are the two isotherm models. The former is associated with monolayer adsorption, in which all of the active sites have the same energy, whereas the adsorption isotherm is Freundlich [49] when heavy metal removal takes place by multilayer adsorption. By fitting the information included in Figs. 10 and 11, which deal with Langmuir and Freundlich isotherms, respectively. We discovered that the R^2 linked to Langmuir values for CuFe₂O₄, Co-CuFe₂O₄ and Zn-CuFe₂O₄ nanoferrites were 0.9800, 0.98008, and 0.9800, respectively, whereas its values for Freundlich were 0.9727, 0.9625, and 0.9790, respectively. The fitted data therefore conform to the Langmuir isotherm model.

The adsorption Kinetics Three models—the interparticle diffusion model, the pseudo first-order model, and the pseudo second-order model—can be used to study the adsorption kinetics. These models are provided by Eqs. (9), (10), and (11) [50, 51]. The physisorption is related to pseudo first order kinetics. There is no chemical link between the adsorbent and the adsorbate in physisorption, which is weak and reversible. While chemisorption adsorption, which is potent and irreversible, is connected to pseudo-second-order kinetics [52, 53, 54, 55, 56, 57]. The intraparticle diffusion kinetic model is the final category of kinetic model. Adsorption happens in a single rate-determining stage in this sort of kinetics, and for the time being, the adsorbate removal is a quick procedure.

From Fitting Figs. 12, 13, 14, it is noticed that The adsorption of Cr(VI) on the surface of MFe₂O₄ (M = Cu, Zn-Cu, and Co-Cu) nanoferrites was followed by the pseudo-second-order kinetic model.

Conclusion

In order to increase the amount of heavy metal ions adsorbed on the adsorbent surface, CuFe₂O₄ was doped with Zn and Co in this work, which is an effective method for increasing the material's physical properties. By using a flash auto combustion process, CuFe₂O₄, Zn-CuFe₂O₄, and Co-CuFe₂O₄ were created, and they all crystallized in a cubic system, as opposed to pure Cu-ferrite, which has a tetragonal crystal structure. Due to its stronger magnetic nature, HRTEM looked into the samples' higher tendency to aggregate. Through BET analysis, the porosity and surface area were investigated. Co-CuFe₂O₄'s surface was where the most gas was adsorbed, while Zn-CuFe₂O₄ provided the most surface area. The behavior of all samples is ferromagnetic. The maximum removal efficiency was donated to CuFe₂O₄ at pH 7, and after 50 min, all investigated samples followed the Langmuir isotherm and pseudosecond-order kinetic models.

Funding Open access funding provided by The Science, Technology & Innovation Funding Authority (STDF) in cooperation with The Egyptian Knowledge Bank (EKB).

Declarations

Conflict of interests The author declare that they have no known conflict of interest or competing financial interests or personal relationships that could have appeared to influence the work reported in this paper 'Effect of (Co and Zn) doping on structural, Characterization and the heavy metal removal efficiency of CuFe₂O₄ Nanoparticles.'

Open Access This article is licensed under a Creative Commons Attribution 4.0 International License, which permits use, sharing, adaptation, distribution and reproduction in any medium or format, as long as you give appropriate credit to the original author(s) and the source, provide a link to the Creative Commons licence, and indicate if changes were made. The images or other third party material in this article are included in the article's Creative Commons licence, unless indicated otherwise in a credit line to the material. If material is not included in the article's Creative Commons licence and your intended use is not permitted by statutory regulation or exceeds the permitted use, you will need to obtain permission directly from the copyright holder. To view a copy of this licence, visit <http://creativecommons.org/licenses/by/4.0/>.

References

1. El-Masry, M. M., Ramadan, R.: Appl. Phys. A. **128**, (2022) <https://doi.org/10.1007/s00339-021-05238-6>
2. Ramadan, R.: Physical study of cobalt ferrite and its application in purification of water. Appl. Phys. A (2019). <https://doi.org/10.1007/s00339-019-3121-8>
3. Singh, N.B., Rachna, K.: Nanotechnology. Monit. Manag. **14**, 100301 (2020). <https://doi.org/10.1016/j.enmm.2020.100301>
4. Ramadan, R., Ismail, A. M.: J. Inorg Organomet Polym Mater. <https://doi.org/10.1007/s10904-021-02176-x>
5. Ramadan, Rania, Almutairi, Fahad N., Alzaidy, Ghada A.: Ceram. Int. **49**, 29520–29533 (2023). <https://doi.org/10.1016/j.ceramint.2023.06.141>
6. Ledari, R.T., Valadi, K., Gharibi, S., Maleki, A.: Mater. Res. Bull. **130**, 110946 (2020). <https://doi.org/10.1016/j.ceramint.2023.06.141>
7. Ramadan, Rania: J. Water Process. Eng **54**, 103958 (2023). <https://doi.org/10.1016/j.jwpe.2023.103958>
8. Tommalieh, M.J., Ismail, A.M., Awwad, N.S., Ibrahim, H.A., Youssef, M.A., Menazea, A.A.: J. Electron. Mater. **49**, 7603 (2020). <https://doi.org/10.1016/j.molstruc.2020.128814>
9. Shafaay, A.S., Ramadan, R.: J. Supercond. Novel Magn. (2023). <https://doi.org/10.1007/s10948-023-06589-2>
10. Naushad, M., Alqadami, A.A., AlOthman, Z.A., Alsohaimi, I.H., Algamdi, M.S., Aldawsari, A.M.: J. Mol. Liq. **293**, 111442. (2019). <https://doi.org/10.1016/j.molliq.2019.111442>
11. Ramadan, R., Ahmed, M.K., El-Masry, M.M.: Polym. Bull. (2023). <https://doi.org/10.1007/s00289-023-04850-1>
12. Ramadan, R., Uskoković, V., El-Masry, M.M.: Journal of Alloys and Compounds **954**, 170040 (2023). <https://doi.org/10.1016/j.jallcom.2023.170040>
13. Ramadan, R., El-Masry, M.M.: Appl. Phys. A. **127**, 876 (2021). <https://doi.org/10.1007/s00339-021-05037-z>
14. Siddiqui, H., Ahmed, K.B.M., Sami, F., Hayat, S.: Springer, Cham (2020). <https://doi.org/10.1016/j.carres.2019.107884>
15. Rogalla, H., Romheld, V.: L. Plant Cell Environ. **25**, 549–555 (2002). <https://doi.org/10.1046/j.1365-3040.2002.00835>

16. Ramadan, R., Ahmed, M.K., El-Masr, M.M.: *Polym. Bull.* (2023). <https://doi.org/10.1007/s00289-023-04850-1>
17. Emam, H.E., El-Shahat, M., Abdelhameed, R.M.: *J. Hazard. Mater.* **414**, 125509 (2021). <https://doi.org/10.1016/j.indcrop.2022.116201>
18. Arman, M.M., Ramadan, R.: *J Mater Sci: Mater Electron* **34**, 1365 (2023). <https://doi.org/10.1007/s10854-023-10721-2>
19. Hafez, R. S., Ramadan, R., El-Khiyami, S.S.: *J. Mater. Sci. Mater Electron.* <https://doi.org/10.1007/s10854-021-06015-0>
20. Shafaay, A.S., Ramadan, R.: *J. Supercond. Nov. Magn.* (2023). <https://doi.org/10.1007/s10948-023-06589-2>
21. Ramadan, R., Ismail, A.M. (2023) <https://doi.org/10.1007/s10904-023-02684-y>
22. Guirguis, O.W., Moselhey, M.T.H.: *J. Mater. Sci.* **46**, 5775 (2011). <https://doi.org/10.4236/ns.2012.41009>
23. Dimitrov, V., Sakka, S.: *J. Appl. Phys.* **79**, 1741 (1996). <https://doi.org/10.1063/1.360962>
24. Ramadan, R., Ismail, A.M.: *Journal of Inorganic and Organometallic Polymers and Materials* (2023). <https://doi.org/10.1007/s10904-023-02684-y>
25. Velsankar, K., Sudhahar, S., Parvathy, G., Kaliammal, R.: *Mater. Chem. Phys.* **239**, 121976 (2020). <https://doi.org/10.1016/J.MATCHEMPHYS.2019.121976>
26. Varaprasad, K., Lopez, M., Núñez, D., Jayaramudu, T., Sadiku, E.R., Karthikeyan, C.: *J. Mol. Liq.* **300**, 112353 (2020). <https://doi.org/10.1016/j.molliq.2019.112353>
27. Thukkaram, M., Cools, P., Nikiforov, A., Rigole, P., Coenye, T., Van Der Voort, P., et al.: *Appl. Surf. Sci.* **500**, 144235 (2020). <https://hdl.handle.net/1854/LU-8583923>
28. Arman, M.M., Ramadan, R., Supercond, J.: *Nov. Magnetism* **33**, 2149–2157 (2020). <https://doi.org/10.1007/s10948-020-05441-1>
29. Azouaoui, A., El Haoua, M., Salmi, S., Benzakour, N., Hourmatallah, A., Bouslykhane, K.: *Comput. Condens. Matter* **23**, 00454 (2020). <https://doi.org/10.1016/j.cocom.2019.e00454>
30. Bharati, V.A., Somvanshi, S.B., Humbe, A.V., Murumkar, V.D., Sondur, V.V., Jadhav, K.M.: *J. Alloys Compd.* **821**, 153501 (2020). <https://doi.org/10.1016/j.jallcom.2019.153501>
31. Ramadan, R., Abdel-Aal, S.K.: *J. Mater. Sci. Mater. Electron.* <https://doi.org/10.1007/s10854-021-06489-y>
32. Ateia, E.E., Abdelamksoud, M.K., Arman, M.M., Ramadan, R., Shafaay, A.S.: *Appl. Phys. A* **125**, 516 (2019). <https://doi.org/10.1007/s00339-019-2815-2>
33. Nakarungseea, S.P., Srirattanapibula, S., Issrob, C., Tangc, I.-M., Thongme, S.: *Sens. Actuat. A* **314**, 112230 (2020). <https://doi.org/10.1016/j.jallcom.2022.165747>
34. Weldegebrieal, G.K.: *Inorg. Chem. Comm.* **120**, (2020). <https://doi.org/10.1016/j.inoche.2020.108140>
35. Chung, Y.T., Mahmoudi, E., Mohammad, A.W., Benamor, A., Johnson, D., Hilal, N.: *Desalination* **402**, 123–132 (2017). <https://doi.org/10.1016/j.desal.2016.09.030>
36. Mohammad, A.W., Hilal, N., Seman, M.N.A.: *Desalination* **158**, 73–78 (2003). <https://doi.org/10.1016/j.desal.2005.02.062>
37. Graves, P.R., Johnston, C., Campaniello, J.J.: *Mater. Res. Bull.* **23**, 1651 (1988). [https://doi.org/10.1016/0025-5408\(88\)90255-3](https://doi.org/10.1016/0025-5408(88)90255-3)
38. Lal, G., Punia, K., Bhoi, H., Dolia, S.N., Choudhary, B.L., Alvi, P.A., Dalela, S., Barbar, S.K., Kumar, S.: *J. Alloys Compd.* **886**, 161190 (2021). <https://doi.org/10.1016/j.jallcom.2021.161190>
39. Lal, G., Punia, K., Dolia, S.N., Alvi, P.A., Dalela, S., Kumar, S.: *Ceram. Int.* **45**(5), 5837–5847 (2019). <https://doi.org/10.1016/j.ceramint.2018.12.050>
40. Lal, G., Punia, K., Dolia, S.N., Alvi, P.A., Choudhary, B.L., Kumar, S.: *J. Alloys Compd.* **828**, 154388 (2020). <https://doi.org/10.1016/j.jallcom.2020.154388>
41. Vincent, E., Dupuis, V., Alba, M., Hammann, J., Bouchaud, J.P.: *EPL (Europhysics Letters)* **50**, 674 (2000). <https://doi.org/10.1209/epl/i2000-00368-1>
42. Chang, H., Guo, Y.-Q., Liang, J.-K., Rao, G.-H.: *J. Magn. Magn. Mater.* **278**, 306 (2004). <https://doi.org/10.1016/j.pmatsci.2013.10.001>
43. Kersten, Z.A.M., Angew, Z.: *Phys* **8**, 496 (1956). [https://doi.org/10.1016/0038-1098\(70\)90266-8](https://doi.org/10.1016/0038-1098(70)90266-8)
44. Bagheri, M., Younesi, H., Hajati, S., Mehdi, S.: *Int. J. Biol. Macromol.* **80**, 431–444 (2015). <https://doi.org/10.1016/j.jenvman.2014.08.022>
45. Chavez-Guajardo, A.E., Medina-Llamas, J.C., Maqueira, L., Andrade, C.A.S., Alves, K.G.B., de Melo, C.P.: *Chem. Eng. J* **281**, 826e836 (2015). <https://doi.org/10.1016/j.cej.2014.08.002>
46. Chen, R., Chai, L., Li, Q., Shi, Y., Wang, Y., Mohammad, A.: *Environ. Sci. Pollut. Res.* **20**, 7175–7185 (2013) 41586-019-1617-1
47. Ramadan, R., Ahmed, M.K.: *Appl. Phys. A* **128**, 1056 (2022). <https://doi.org/10.1007/s00339-022-06197-2>
48. Shen, H., Pan, S., Zhang, Y., Huang, X., Gong, H.: *Chem. Eng. J.* **183**, 180–191 (2012). <https://doi.org/10.1016/j.pmatsci.2013.10.001>
49. Ismail, A.M., Ramadan, R., El-Masry, M.M.: *J. Aust. Ceram. Soc.* (2023). <https://doi.org/10.1007/s41779-023-00836-4>
50. Ramadan, R.: *Appl. Phys. A* **125**, 825 (2019). <https://doi.org/10.1007/s00339-019-3121-8>
51. Oliveira, V.H.B., Rechetnek, F., da Silva, E.P., de Sousa Marques, V., Rubira, A.F., Silva, R., Lourenc, S.A., Muniz, E.C.: *J. Mol. Liq* **309**, 113041 (2020). <https://doi.org/10.1111/j.1601-183X.2008.00439.x>
52. Ramadan, R.: *Appl. Phys. A* **129**, 125 (2023). <https://doi.org/10.1007/s00339-022-06376-1>
53. Zhao, Y.-G., Shen, H.-Y., Pan, S.-D., Hu, M.-Q., Xia, Q.-H.: *J. Mater. Sci.* **45**, 5291–5301 (2010). <https://doi.org/10.1016/j.actamat.2019.12.015>
54. El-Masry, M.M., El-Razek Mahmoudb, A., Morshidyc, H.Y., Ramadan, R.: (2023). <https://doi.org/10.1007/s10854-022-09777-3>
55. Kaya, I.G.B., Duranoglu, D., Beker, U., Senkal, B.F.: *Clean.-Soil, Air, Water* **39**, 980–988 (2011). <https://doi.org/10.1002/clen.201000552>
56. Li, J., Kalam, A., Al-shihri, A.S., Su, Q., Zhong, G., Du, G.: *Mater. Chem. Phys.* **130**, 1066–1071 (2011). <https://doi.org/10.1016/j.ijmecs.2022.108026>
57. Zhu, H., Jia, S., Wan, T., Jia, Y., Yang, H., Li, J., Yan, L., Zhong, C.: *Carbohydr. Polym.* **86**, 1558–1564 (2011). <https://doi.org/10.1007/s10570-019-02446-5>

Publisher's note Springer Nature remains neutral with regard to jurisdictional claims in published maps and institutional affiliations.